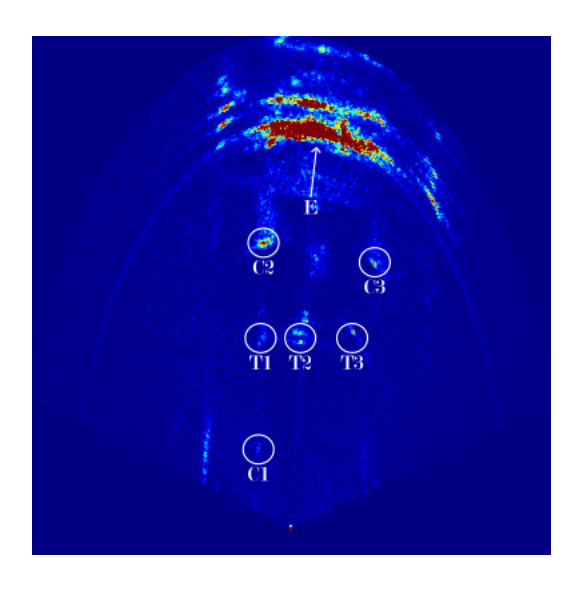


Synthetic Aperture Radar for Automated Guided Carts

Julian Kruse



A thesis presented for the degree of Bachelor of Science

Fakultät Technik und Informatik Hochschule für Angewandte Wissenschaften Hamburg Germany 10.09.2024

Julian Kruse

Synthetic Aperture Radar for Automated Guided Carts

A thesis presented for the degree of Bachelor of Science in the study course B.Sc. Elektro- und Informationstechnik at the department Informations- und Elektrotechnik at the faculty Technik und Informatik at Hochschule für Angewandte Wissenschaften Hamburg

First supervisor: Prof. Dr. Matthias Kronauge Second supervisor: Prof. Dr. Lutz Leutelt

Submitted on: 10.09.2024

Abstract

The rise of autonomous guided carts (AGCs), such as robot vacuum cleaners and lawnmowers, and their increasingly sophisticated navigation systems have led to an increased demand for effective perception of their surroundings. The synthetic aperture radar (SAR) imaging method, which has been successfully employed in airborne and spaceborne applications, is now being introduced to the automotive sector as well as robotics. In light of the recent developments, it seems that synthetic aperture radar (SAR) for automated guided carts (AGCs) may prove to be a valuable asset for imaging. This thesis proposes, simulates, and tests a low-speed and short-range, side-looking (SL) synthetic aperture radar (SAR) procedure for use in automated guided carts (AGCs). In order to potentially increase miniaturization, a single-input single-output (SISO) frequency modulated continuous wave (FMCW) radar system with a transmitter frequency of 60 GHz is employed. The proposed procedure is capable of producing sufficiently resolute images in both free-field and high-clutter conditions.

Die aktuellen Fortschritte im Bereich autonomer Kleinfahrzeuge (AGCs) wie Saugroboter und Rasenmähroboter mit zunehmend komplexeren Navigationssystemen erfordern effektive bildgebende Verfahren zur Erfassung ihrer Umgebung. Das üblicherweise in Raum- und Luftfahrt eingesetzte Synthetic Aperture Radar (SAR) verspricht hochauflösende Bilder und ist Gegenstand aktueller Forschung im Bereich der Automobilentwicklung sowie der Robotik. Die Anwendung von Synthetic Aperture Radar (SAR) auf autonome Kleinfahrzeuge (AGCs) könnte sich als eine wertvolle Ergänzung zur bildgebenden Sensorik dieser herausstellen. In dieser Thesis wird ein auf autonome Kleinfahrzeuge zugeschnittener Synthetic Aperture Radar (SAR) Algorithmus für geringe Geschwindigkeit und Reichweite vorgestellt, simuliert und getestet. Aus Gründen der Miniaturisierbarkeit wird ein 60 GHz Radar, das lediglich einen Transmitter und einen Empfänger (SISO) nutzt, verwendet. Der vorgestellte Algorithmus ist in der Lage, ausreichend aufgelöste Bilder bei Freifeld- und durch Clutter gestörten Bedingungen zu produzieren.

Keywords

SAR, synthetic aperture radar, FMCW, IWR6843ISK, DCA1000, AGC, automated guided cart, Imaging, Radar, Image formation, SISO, side-looking, short range, low velocity, robot, navigation, focusing, migration, correction, windowing, signal processing, FFT, test, room scan, coordinate transformation, grid transformation, polar coordinates

Stichworte

SAR, synthetic aperture radar, FMCW, IWR6843ISK, DCA1000 AGC, autonome Kleinfahrzeuge, Bildgebung, Radar, Bilderzeugung, SISO, Nahbereich, Roboter, Navigation, Fokussierung, Schärfung, Verzerrung, Korrektur, Fensterung, Signal Verarbeitung, FFT, Test, Raumscan, Koordinatentransformation, Rastertransformation, Polarkoordinaten

Contents

Abstract										
List of Figures										
List of Tables										
\mathbf{A}	bbre	viation	s XI							
1	Intr	oducti	on 1							
2	SAI	ring 3								
	2.1	Defini	tions and Assumptions							
	2.2	Synth	etic Aperture Radar Fundamentals 5							
		2.2.1	Distance Measurement Principle							
		2.2.2	Angular Measurement Principle 5							
		2.2.3	Synthetic Aperture Principle 6							
	2.3	FMCV	V Radar and Baseband Signal 8							
	2.4									
		2.4.1	Waveform Description							
		2.4.2	Sampling Pattern							
		2.4.3	Data Matrix Construction							
		2.4.4	Resulting Baseband Signal							
	2.5	Image	Formation							
		2.5.1	Range Compression							
		2.5.2	Azimuth Compression							
		2.5.3	Combined Compression							
		2.5.4	Grid and Position Relationship							
		2.5.5	Maximum Unambiguous Range and Angle 15							

VI	CONTENTS
----	----------

		2.5.6	Range and Angle Bin Size	16					
		2.5.7	Windowing	16					
	2.6	Transfe	ormation to Cartesian Image	18					
		2.6.1	Grid Limits	19					
		2.6.2	Grid Bin Size	19					
		2.6.3	Transformation	19					
		2.6.4	Transformation Characteristics	20					
	2.7	Focusi	ng	21					
		2.7.1	Migration prediction	21					
		2.7.2	Migration Correction	23					
	2.8	Result	ing Signal Processing Algorithm	24					
•				a -					
3		lysis		27					
	3.1		are and proposed system settings	27					
		3.1.1	Radar sensor	27					
		3.1.2	Platform	27					
		3.1.3	Resulting SAR Capabilities	28					
	3.2	Simulation		29					
		3.2.1	Targets	29					
		3.2.2	Results	30					
	3.3	-	mental Results	34					
		3.3.1	Entrance Hall Measurement	34					
		3.3.2	Hallway Measurement	34					
4	Con	clusion	า	37					
-	4 Conclusion								
Bi	bliog	raphy		39					
\mathbf{St}	atem	ent of	Independence	41					
\mathbf{A}	Sens	sor set	tings	43					

List of Figures

2.1	Application Concept	3
2.2	Parameter Definitions	4
2.3	Wave Propagation Distance	5
2.4	Geometric Relation of Target Angle and radial Velocity	6
2.5	Doppler Effect and Frequency	6
2.6	SAR Measurement Principle	7
2.7	Real and Synthetic Aperture	7
2.8	Transmitted and received Chirp Sequence Waveform	9
2.9	Sampling Moments Situated in Waveform	9
2.10	Sampling of Baseband and Matrix Creation	10
2.11	Matrix of Baseband Signal	12
2.12	Matrix of Range Compressed Baseband Signal	13
2.13	Matrix of Azimuth Compressed Baseband Signal	14
2.14	Matrix of Range and Azimtuh Compressed Baseband Signal .	15
2.15	Image Grid (Range-Angle)	17
2.16	Spectra of Window Functions	17
2.17	Target Appearance in Range-Angle and X-Y Domain	18
2.18	Mapping of Grid Points to X-Y Domain	20
2.19	Transformation Characteristics	21
2.20	Distortion due to Range and Angle Migration	22
2.21	Range and Angle Migration Geometry	22
2.22	Focusing Algorithm Concept	24
2.23	Signal Processing Overview	25
3.1	Sensor Platform	28
3.2	Simulation Setup	30
3.3	Simulation of Single Target	31
3.4	Simulation of Multiple Targets	32

VIII	LIST OF FIGURE	S
3.5	Application of Focusing	3
3.6	Entrance Hall Measurement Result	5
3.7	Hallway Measurement Result	6

List of Tables

3.1	Simulation and Sensor Parameters				•		•	28
A.1	Proposed Sensor Parameters							44
A.2	Theory Parameters and Sensor Parameters							45

Abbreviations

SAR Synthetic Aperture Radar

RAR Real Aperture Radar

AGC Automated Guided Cart

SL Side-looking

SISO Single Input Single Output

FMCW Frequency Modulated Continuous Wave

Rx Receiver

Tx Transmitter

BB Baseband

DFT Discrete Fourier Transform

FFT Fast Fourier Transform

ADC Analog-to-digital Converter

Chapter 1

Introduction

The use of automated guided carts (AGCs), such as vacuum cleaners, lawn-mowers, and delivery robots, is becoming increasingly prevalent in both households and the logistics industry. [1] [2] The automated guidance of AGCs relies on sensors to perceive the environment. In order to facilitate a more sophisticated guidance of AGCs, a detailed perception of the environment is required. [2]

Radar sensors are typically utilized in large-scale applications, including airport towers, maritime vessels, and aircraft. Such systems permit the perception of the surrounding environment. These conventional radar systems typically employ an aperture of sensors, which is referred to as a Real Aperture Radar (RAR). An increase in aperture size allows for a higher-resolution image of the environment. In contrast, for applications of a smaller scale, the aperture size is constrained by the dimensions of the sensor platform. In the field of aerospace, this contradiction has been partly resolved through the introduction of Synthetic Aperture Radar (SAR). Rather than increasing the aperture size, the platform movement is exploited to create the effect of an increased aperture size. [3] The enhanced miniaturization may prove advantageous for ground-based SAR applications.

A number of studies have been conducted on ground-based SAR in the automotive and locomotive sector, including the works [4], [5], [6], [7], and [8]. These typically address higher platform velocities and longer synthetic apertures than those applicable to AGCs.

The objective of this thesis is to apply the SAR algorithm to AGCs to benefit from decreased aperture size. To prove the concept, a side-looking, single-input single-output synthetic aperture radar (SL SISO SAR) imaging algorithm for a slow-moving ($< 30 \frac{cm}{s}$) ground vehicle using a millimeter frequency modulated continuous wave (mmFMCW) radar is developed to produce an image within 30m.

In 2023 a forward-looking SAR algorithm for AGCs using multiple transmitter and receiver channels was introduced in the cited work [2]. The approach of this thesis differs from that presented in [2] in that the proposed algorithm is designed for side-looking SAR and only uses a single transmitter and receiver channel (SISO).

The thesis introduces the proposed SAR algorithm in chapter 2. In the following analysis (chapter 3), the proposed algorithm is simulated and applied to an AGC. Finally, the conclusions are drawn in chapter 4.

Chapter 2

SAR imaging

In order to derive the SAR algorithm, first the necessary definitions and assumptions are clarified. (section 2.1). Subsequently, section 2.2 elucidates the foundational principles of SAR measurements. Then follows an introduction to the utilized Radar technology (section 2.3) as well as waveform design and sampling method 2.4. That allows an understanding of the image formation (section 2.5). Lastly, the image focusing will be discussed (section 2.7). A comprehensive overview can be found in section 2.8. This thesis focuses on a scenario as depicted in figure 2.1.

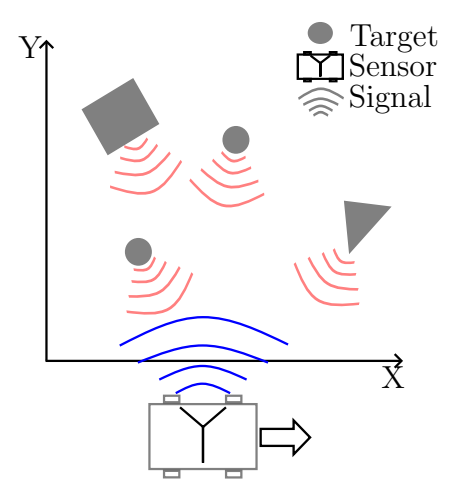


Figure 2.1: A mobile platform moves, carrying a sideways-mounted Radar. A signal is emitted by the radar (blue) and reflects on the targets (red).

2.1 Definitions and Assumptions

It is essential to elucidate three pivotal parameters. These are illustrated in figure 2.2. The sensor platform velocity v_P is defined as the velocity of the sensor platform relative to the ground. The radial velocity between the sensor platform and the target, designated as v_r , is the sum of the vector components of the platform and target velocity oriented towards the target. The target angle α is defined with respect to the sensor alignment. A target situated directly in front of the sensor is at target angle $\alpha = 0^{\circ}$. Targets that are located on the right-hand side of the sensor have a positive target angle.

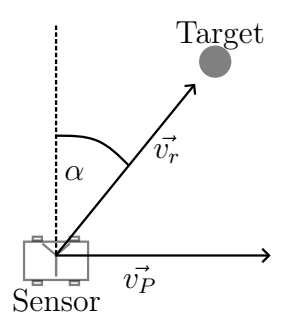


Figure 2.2: Platform speed, radial velocity, and target angle.

In order to apply the SAR algorithm to AGCs, a number of assumptions have been made, which are outlined below:

- 1. The sensor is mounted in a precise lateral alignment with the direction of movement of the platform. This configuration ensures optimal results for SAR. [3].
- 2. The sensor platform is in a state of constant motion along a straight trajectory. This implies that no acceleration occurs, and the platform's speed, v_P , is time-independent.
- 3. The platform velocity is low $v_P < 30 \frac{cm}{s}$ and the relevant target distances are $R_0 < 30m$.
- 4. All relevant targets are static in position so that the radial velocity v_r is only a component of the platform velocity v_P .

2.2 Synthetic Aperture Radar Fundamentals

Radars in general comprise a transmitter and an aperture of at least one receiver. The transmitter emits an electromagnetic wave, which is reflected by a target. This results apart from a change in amplitude, in a time delay, frequency shift, and phase shift between the emissioned and reflected wave at each receiver. The measurement of these effects allows for the location of the target [3]. The target position is determined by the distance R_0 and angle α between the radar and the target.

2.2.1 Distance Measurement Principle The range to target R_0 can be obtained by measuring the propagation time τ of a wave from a transmitter to a receiver. The wave propagates twice the distance to the target at the speed of light c (see figure 2.3). Hence R_0 is calculated [3] [9]

$$R_0 = c \cdot \frac{\tau}{2} \,. \tag{2.1}$$

The maximum range and range resolution are contingent upon the technology parameters that will be discussed in subsequent sections.

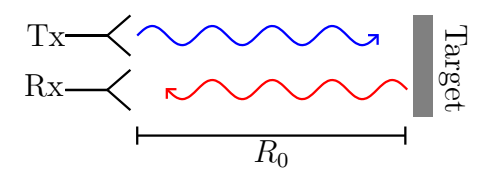


Figure 2.3: The transmitted (blue) and reflected (red) waves both propagate the target distance.

2.2.2 Angular Measurement Principle Following the fourth assumption in section 2.1 the radial velocity v_r is only a component of the platform velocity v_P . Knowing the trajectory of the sensor platform will then allow relating the radial velocity between the sensor and target v_r with the target angle α . That is (see figure 2.4) [3]

$$v_r = v_P \cdot \sin(\alpha). \tag{2.2}$$

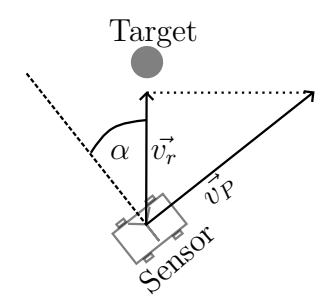


Figure 2.4: Geometry for relating target angle α , radial velocity v_r and platform velocity v_P .

The equation demonstrates that, given the values of the radial velocity v_r and the platform velocity v_P , the target angle α can be calculated. To measure the radial velocity, the *Doppler effect* can be exploited. If the platform is moving towards the target, the signal frequency increases; if the platform is moving away, the signal frequency decreases (see figure 2.5). The change in frequency is called the Doppler frequency f_D and can be calculated as follows [3]

$$f_D = -\frac{2v_r}{c} \cdot f_0 = -\frac{2v_P \cdot \sin(\alpha)}{c} \cdot f_0.$$
 (2.3)

Where f_0 denotes the signal frequency. The measurement of the Doppler frequency f_D is discussed in section 2.4.4.

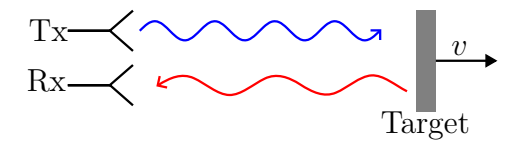


Figure 2.5: The transmitted (blue) and reflected (red) frequencies are distinct due to the Doppler effect.

The maximum angle is determined by technological parameters, which will be discussed in greater detail at a later point. The angular resolution is dependent on the radar's aperture length, which, in this thesis, is synthetic.

2.2.3 Synthetic Aperture Principle Real aperture radars (RAR) employ an aperture comprising multiple receivers. The aperture length is the

pivotal parameter for enhancing angular resolution. In the case of a single-input, single-output (SISO) synthetic aperture radar (SAR), the necessity for a physical aperture is negated, resulting in minimal spatial requirements. [3] SAR utilizes the sensor movement to create a so-called synthetic aperture. The designation "synthetic" is applied to this method because it employs signal processing to generate measurements that are similar to those obtained through RAR. [3]

As depicted in figure 2.6, snapshots of the reflected wave are taken along the sensor's path. The one receiver spans up an aperture with the implication of a changing transmitter position over time.[3] A conceptual comparison between RAR and SAR can be found in figure 2.7.

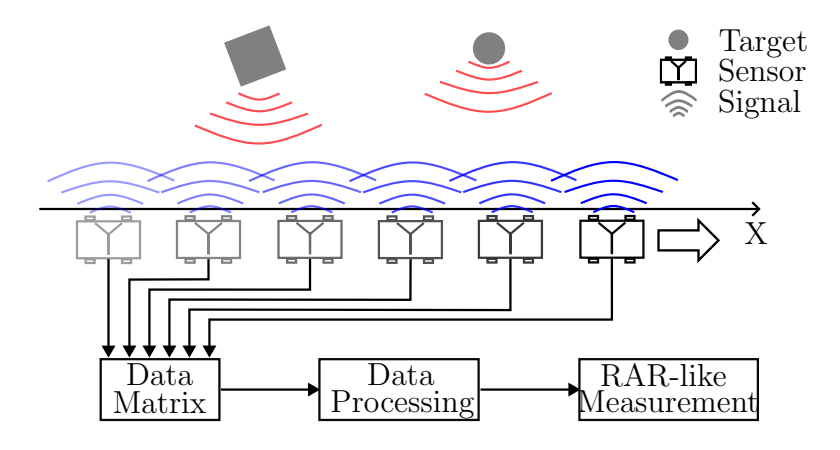


Figure 2.6: Snapshots of the targets are taken along the sensor's path. Data processing allows for the imitation of RAR measurements.

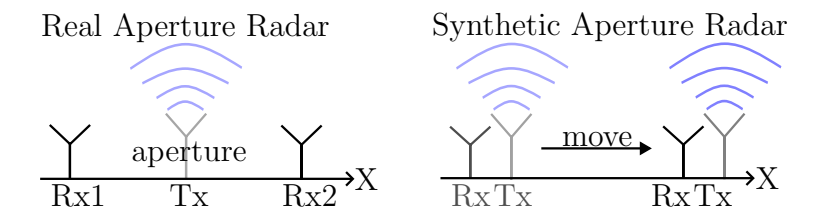


Figure 2.7: Incoming waves are measured by one transmitter and two receivers on a real aperture (left) and one transmitter and one receiver forming a synthetic aperture (right).

The following sections present the technology employed to provide a more detailed account of the measurement of target range and angle.

2.3 FMCW Radar and Baseband Signal

This thesis employs a frequency-modulated (FM) continuous wave (CW) radar system. FMCW radars utilize a continuous emission of electromagnetic waves, which are then reflected by surrounding objects and subsequently received by the radar. The emission signal is frequency-modulated.

By means of a continuous comparison between the transmitted signal $s_T(t)$ and the received signal $s_R(t)$ it is possible to obtain the so-called baseband signal $s_R(t)$. Further details on this approach can be found in the cited work [9].

The baseband signals frequency and phase contain information about the target locations. The design of the waveform of the transmission signal $s_T(t)$ and the sampling of the baseband signal $s_B(t)$ determine which information about the target is contained.[9]

Subsequently, the utilized waveform and sampling methodology will be elucidated, after which the baseband signal can be elaborated upon in comprehensive detail.

2.4 Waveform Design and Sampling

There are several waveform designs with different properties. [9] In view of the potential for simultaneously acquiring both range and angle data, a linear chirp sequence waveform will be employed in this thesis. [9]

2.4.1 Waveform Description A chirp sequence is comprised of a series of identical chirps, each with a duration of T_{chirp} and a linear chirp ramp with bandwidth B_{sw} . The starting frequency f_0 is maintained throughout the sequence. Figure 2.8 illustrates the transmitted chirp sequence and the received chirp sequence affected by a delay and a frequency shift.

It is important to note that the shape of the chirp sequence, including factors such as steepness, starting delays, delays between chirps, and others, is affected by technical limitations.

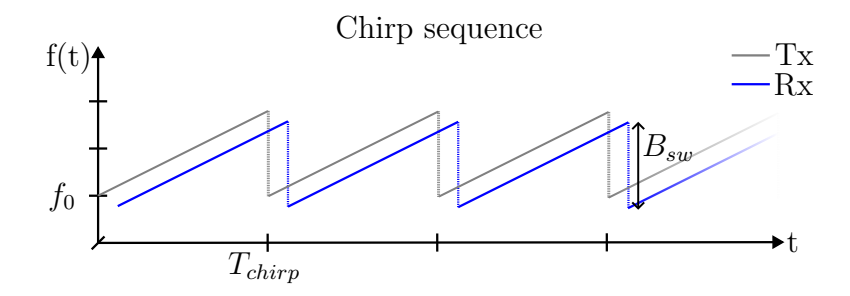


Figure 2.8: The transmitted (grey) and received (blue) Chirp Sequence Waveform

2.4.2 Sampling Pattern The baseband signal is sampled at two distinct rates as depicted in figure 2.9. The slower sampling rate is employed to obtain data across the entire chirp sequence of Length N-1, with a sampling interval of T_{chirp} . Sampling occurs when the individual chirp n ramp attains a specific frequency. Consequently, if delays between the chirps are used, the delay will be added to this sampling time.

The faster sampling rate is employed to gather data within the time interval of one individual chirp n in the chirp sequence of length N-1. This sampling time is designated as T_r .

The dimension of faster sampling will be designated as *intra-chirp*, while the slower sampling time will be referred to as *inter-chirp*.

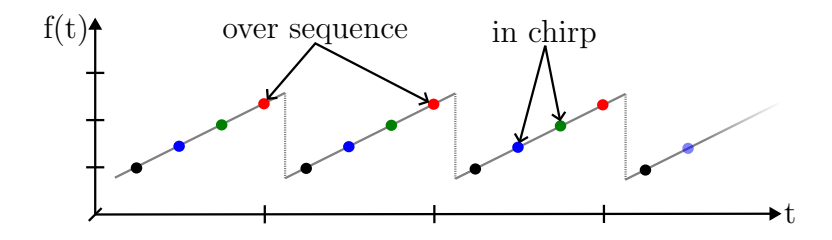


Figure 2.9: Moments of sampling situated in the chirp sequence. Note that the baseband signal and not the received signal is sampled.

2.4.3 Data Matrix Construction The sampled data is stored in a $N \times M$ matrix. An illustration of the sampling and data matrix is situated in figure 2.10. The variable n is an integer in the interval $0 \dots N-1$ and refers to the

inter-chirp dimension. For instance, index n=2 would refer to the third chirp in the sequence.

Each chirp is measured with M samples with a sampling time of T_r so that $T_{chirp} = MT_r$. Here m is an integer in the interval $0 \dots M-1$ and refers to the *intra-chirp* dimension. In this manner, all samples of the third chirp of the sequence can be referred to as (m, n = 2). This data matrix is the format utilized for signal processing.

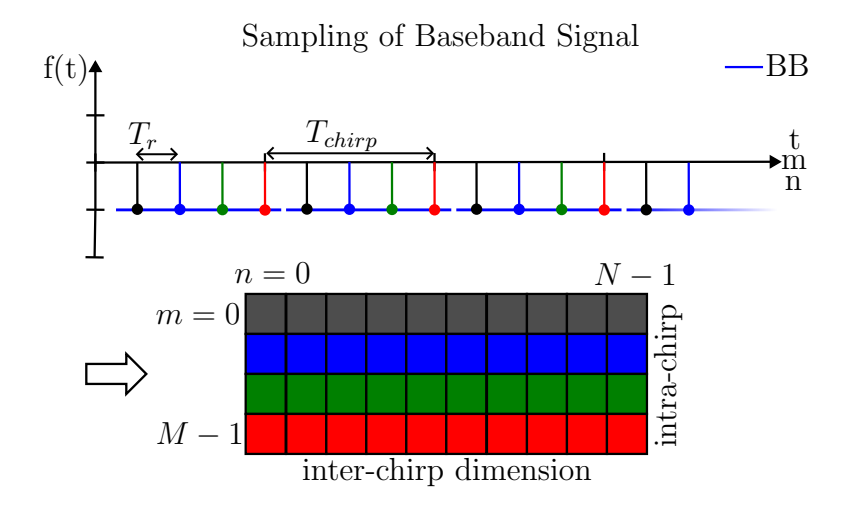


Figure 2.10: Sampling of the baseband signal and construction to a data matrix.

2.4.4 Resulting Baseband Signal As outlined in section 2.3, the baseband signal is the product of comparing the emissioned and received wave. Assuming $B_{sw} \ll f_0$ and using the introduced waveform design and sampling method, the baseband signal $s_B(m,n)$ for one target can be described as

$$s_B(m,n) = exp(j2\pi(f_B m T_r + f_D n T_{chirp} + \Phi_0))$$
 (2.4)

with the beat frequency f_B , the Doppler frequency f_D and the phase component Φ_0 . A derivation can be found in the cited work [9].

Doppler Frequency The Doppler frequency f_D is directly related to the radial velocity to the target and therefore to the target angle and platform

velocity. (see equation 2.2)

$$f_D = -f_0 \frac{2v_r}{c} = -f_0 \frac{2v_P sin(\alpha)}{c}$$
(2.5)

It depends on index n, so the target angle corresponds to the inter-chirp dimension. That means the sampling time for the target angle is T_{chirp} .

Beat Frequency The beat frequency f_B has a Doppler component and a range component. [9] With the assumed low speed (section 2.1) the Doppler component can be neglected so that

$$f_B = f_D + f_\tau = -f_0 \frac{2v_r}{c} - \frac{B_{sw}}{T_{chirp}} \frac{2R_0}{c}$$

$$\approx f_\tau = -\frac{B_{sw}}{T_{chirp}} \frac{2R_0}{c} .$$
(2.6)

The beat frequency depends on index m, so the target range corresponds to the intra-chirp dimension. The sampling time for the target range is T_r . It should be noted that the beat frequency is scaled by the chirp slope $\frac{B_{sw}}{T_{chirp}}$.

Phase Component The phase component is independent of the sampling variables and is therefore irrelevant in the context of this thesis.

$$\Phi_0 = -f_0 \frac{2R_0}{c} \tag{2.7}$$

2.5 Image Formation

The baseband signal frequency has a range component that is only present in the intra-chirp dimension and an angle component that is present in the inter-chirp dimension.

Performing a DFT on the signal sequence yields its spectrum and allows the separation of targets. This is because of the direct relationship between beat frequency f_B and distance R_0 (equation 2.6) as well as Doppler frequency f_D and angle α (equation 2.5). The baseband signal of a single point target may be represented by a signal of the form illustrated in Figure 2.11. Now, performing a DFT in both intra-chirp and inter-chirp dimension will be discussed.

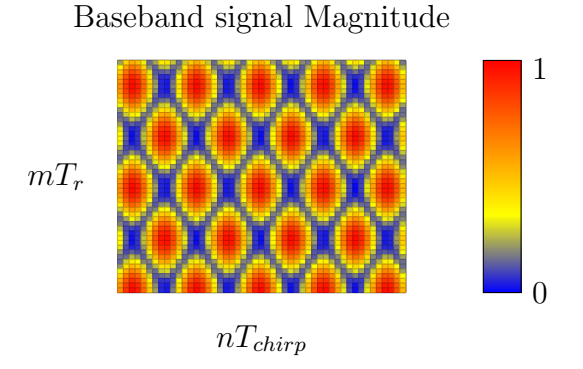


Figure 2.11: Possible baseband signal of a single point target.

2.5.1 Range Compression The spectrum of the sequence $s_B(m,n)$ in intra-chirp dimension mT_r is

$$S_{B}(k,n) = DFT_{m} \{s_{B}(m,n)\}$$

$$= \sum_{m=0}^{M-1} e^{j2\pi(f_{\tau}mT_{r} + f_{D}nT_{chirp} + \Phi_{0})} e^{-j2\pi \frac{mk}{M}}$$

$$= e^{j2\pi(f_{D}nT_{chirp} + \Phi_{0})} \cdot \sum_{m=0}^{M-1} e^{j2\pi m(f_{\tau}T_{r} - \frac{k}{M})}$$

$$= e^{j2\pi(f_{D}nT_{chirp} + \Phi_{0})} \cdot \begin{cases} M & \text{for } \frac{k}{M} = f_{\tau}T_{r} \\ \sum_{m=0}^{M-1} e^{j2\pi m(f_{\tau}T_{r} - \frac{k}{M})} & \text{else} \end{cases}$$

$$(2.8)$$

using the DFT with k as the discrete frequency index. There is a maximum in magnitude for $\frac{k}{M} = f_{\tau}T_{r}$. Due to the distance relation, this step is called the range compression. It is considered a compression because a wave of a specific frequency is compressed into a single peak. A visualization of the range compression can be found in figure 2.12.

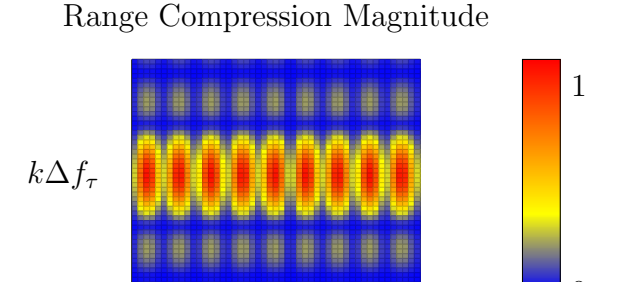


Figure 2.12: Possible range compressed baseband signal of a single point target.

 nT_{chirp}

2.5.2 Azimuth Compression The spectrum of sequence s_B in the interchirp dimension nT_{chirp} is

$$S_{B}(m,l) = DFT_{n}\{s_{B}(m,n)\}$$

$$= \sum_{n=0}^{N-1} e^{j2\pi(f_{\tau}mT_{r} + f_{D}nT_{chirp} + \Phi_{0})} e^{-j2\pi \frac{ml}{N}}$$

$$= e^{j2\pi(f_{\tau}mT_{r} + \Phi_{0})} \cdot \sum_{n=0}^{N-1} e^{j2\pi n(f_{D}T_{chirp} - \frac{l}{N})}$$

$$= e^{j2\pi(f_{\tau}mT_{r} + \Phi_{0})} \cdot \begin{cases} N & \text{for } \frac{l}{N} = f_{D}T_{chirp} \\ \sum_{n=0}^{N-1} e^{j2\pi n(f_{D}T_{chirp} - \frac{l}{N})} & \text{else} \end{cases}$$

$$(2.9)$$

using the DFT with l as the discrete frequency index. Here a maximum can be observed when $\frac{l}{N} = f_D T_{chirp}$. This step is referred to as azimuth compression because of the angle relation. This is visualized in figure 2.13.

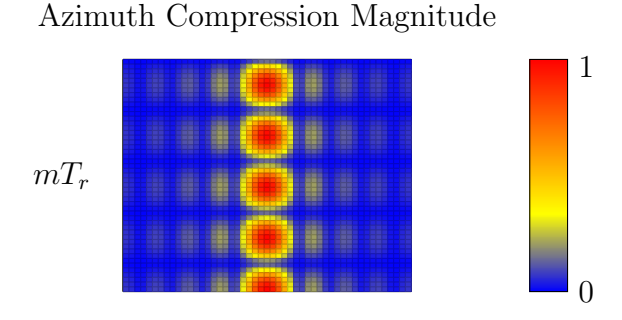


Figure 2.13: Possible azimuth compressed baseband signal of a single point target.

 $l\Delta f_D$

2.5.3 Combined Compression Combining the two procedures leads to the 2D-DFT of $s_B(m, n)$.

$$S_{B}(\frac{k}{M}, \frac{l}{N}) = DFT_{m,n}\{s_{B}(m, n)\}$$

$$= \sum_{m=0}^{M-1} \sum_{n=0}^{N-1} s_{B}(m, n)e^{-j2\pi \frac{nl}{N}}e^{-j2\pi \frac{mk}{M}}$$

$$= e^{j2\pi\Phi_{0}} \sum_{m=0}^{M-1} e^{j2\pi m(f_{\tau}T_{r} - \frac{k}{M})} \sum_{n=0}^{N-1} e^{j2\pi n(f_{D}nT_{r} - \frac{l}{N})}$$

$$= e^{j2\pi\Phi_{0}} \cdot \begin{cases} M \cdot N & \text{for } (\frac{k}{M} = f_{\tau}T_{r}) \wedge (\frac{l}{N} = f_{D}T_{chirp}) \\ \sum_{m=0}^{M-1} e^{j2\pi m(f_{\tau}T_{r} - \frac{k}{M})} \sum_{n=0}^{N-1} e^{j2\pi n(f_{D}nT_{r} - \frac{l}{N})} & \text{else} \end{cases}$$

$$(2.10)$$

using the DFT with k as the discrete frequency index corresponding to the intra-chirp component m, and l as the discrete frequency index corresponding to the inter-chirp component n. There is a maximum if both previously discussed conditions are met. (see figure 2.14)

A target appears as a maximum on a point in the two-dimensional spectrum that is related to the target position. This is what makes the spectrum $S_B(k,l)$ an image. To efficiently compute the 2D-DFT, first, a Fast Fourier Transform (FFT) can be performed on the data matrix $s_B(m,n)$. This is followed by a second FFT on the transposed result of the first step.

Combined Compression Magnitude

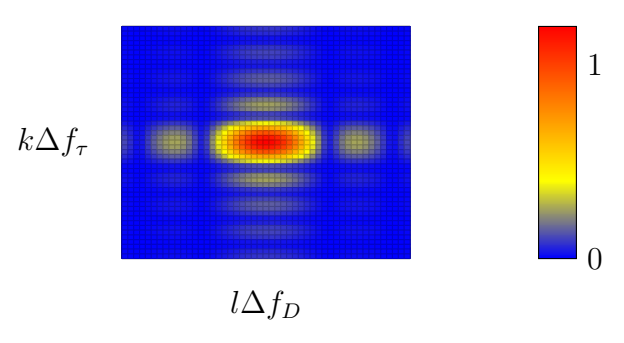


Figure 2.14: Possible range and azimuth compressed baseband signal of a single point target.

2.5.4 Grid and Position Relationship The beat frequency $f_B(k, l)$ corresponds to the target range in k dimension (see equation 2.6)

$$R_0(k) \approx -\frac{T_{chirp}}{B_{evo}} \cdot \frac{c}{2} \cdot k\Delta f_{\tau} \,.$$
 (2.11)

Similarly, each index l corresponds to an angle bin with the relation (see equation 2.3)

$$\alpha(l) = \sin^{-1}\left(-\frac{c}{2v_P f_0} \cdot l\Delta f_D\right). \tag{2.12}$$

The possible mapped frequencies $k\Delta f_{\tau}$ and $l\Delta f_{D}$ can be determined by identifying the maximum unambiguous frequencies and their bin sizes on the DFT spectrum.

2.5.5 Maximum Unambiguous Range and Angle According to the sampling theorem the maximum unambiguous frequencies on the DFT spectrum are:

$$f_{max} = \pm \frac{F_s}{2} = \pm \frac{1}{2T_s} \,. \tag{2.13}$$

With F_s being the sampling frequency and T_s the sampling time.

To calculate the maximum unambiguous range this can be inserted into equation 2.11 which yields

$$R_{0,max} \approx -\frac{T_{chirp}}{B_{sw}} \cdot \frac{c}{2} \cdot \left(\pm \frac{1}{2T_r}\right)$$
 (2.14)

The maximum unambiguous angle can be calculated in the same way using equation 2.12.

$$\alpha_{max} = \sin^{-1} \left(-\frac{c}{2v_P f_0} \cdot \left(\pm \frac{1}{2T_{chirp}} \right) \right). \tag{2.15}$$

It is crucial to recognize that both range and angle are influenced not only by sampling rates but also by the waveform design, sampling and platform speed.

2.5.6 Range and Angle Bin Size A DFT spectrum has the bandwidth of $2f_{max} = F_s$. The number of samples N_s equals the number of frequency bins so that

$$\Delta f = \frac{F_s}{N_s} \tag{2.16}$$

Using this on equation 2.11 leads to the size of range bins

$$\Delta R_0 \approx -\frac{T_{chirp}}{B_{sw}} \cdot \frac{c}{2} \frac{1}{MT_R} \,. \tag{2.17}$$

Following this procedure, the size of the angle bins becomes (see equation 2.12)

$$\Delta \alpha = \sin^{-1} \left(-\frac{c}{2v_P f_0} \cdot \frac{1}{N T_{chirp}} \right)$$

$$= \sin^{-1} \left(-\frac{c}{2f_0} \cdot \frac{1}{D_P} \right). \tag{2.18}$$

 D_P denotes the distance traversed by the platform over the course of the measurement. This quantity can be understood as the synthetic aperture length, which has a direct impact on the angular bin size.

The maximum unambiguous range and angle as well as the range and angle bins lead to the image grid visualized in figure 2.15.

2.5.7 Windowing Due to the limited set of data points, the baseband signal is affected by a window function. This produces non-zero values at other frequencies than the actual frequency of the observed wave [10]. In the context of synthetic aperture radar (SAR) imagery, this results in interference between targets on the image. A reason for this phenomenon is the so-called

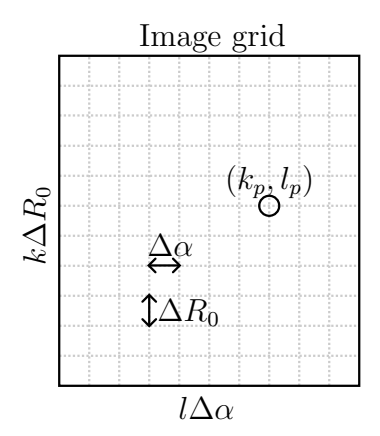


Figure 2.15: Image grid after image formation.

leakage effect. Several window functions can be used to change the properties of the interferences by reducing the leakage effect. [10]

The Dolph-Chebyshev window offers an adjustable equiripple condition on its sidelobes, which results in a reduction in interference between targets throughout the image. A comparison between rectangular (unedited measurement) and Dolph-Chebyshev window with -60dB sidelobes is shown in figure 2.16. The Dolph-Chebyshev window needs to be multiplied in both dimensions with the unprocessed data $s_B(m, n)$ in the time domain.

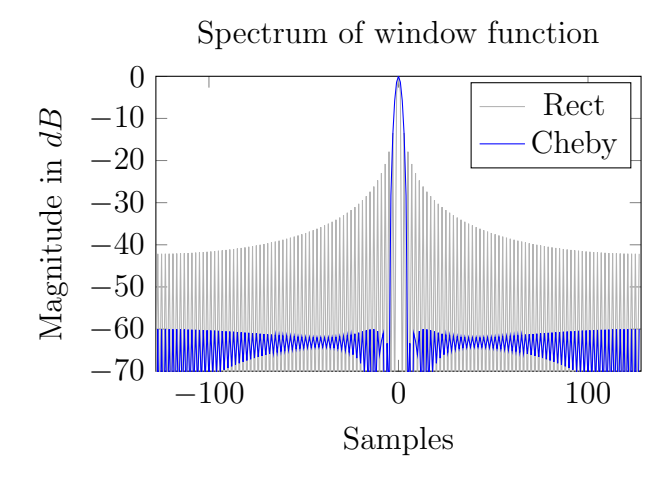


Figure 2.16: Spectra of the rectangular and Dolph-Chebyshev window functions.

2.6 Transformation to Cartesian Image

The cartesian domain is a more intuitive format for the analysis of images than the range-angle domain. As illustrated in figure 2.17 b), the grid-like positioning of targets (figure 2.17 a)) appears distorted without a transformation to cartesian coordinates. Furthermore, the shapes of objects might be unrecognizable. Such a transformation can be done according using the

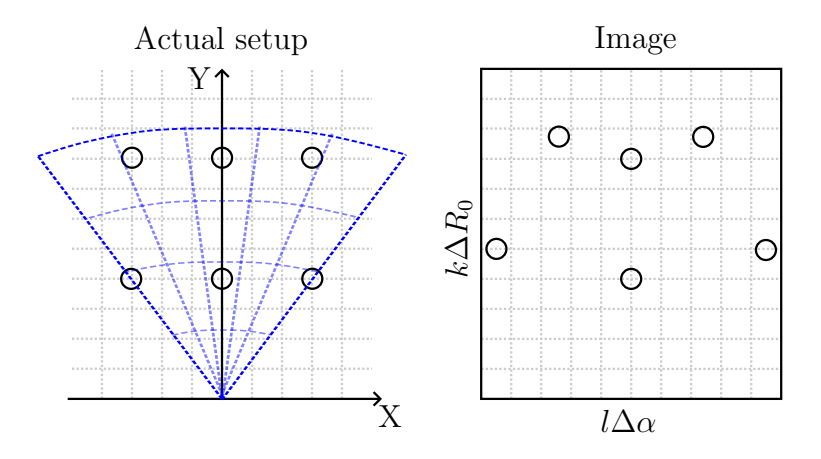


Figure 2.17: Appearance of a grid-like positioning of point targets in the range-angle domain.

transformation from polar to cartesian coordinates. The procedure can be conceptualized as a remapping of points with their values to their corresponding points in the X-Y domain. The challenge lies in identifying an appropriate X-Y grid to correctly position the data points within it.

Every point (k, l) in the grid of $S_B(k, l)$ represents a certain range and angle as described in equation 2.11 and 2.12. So every point (k, l) can be translated to X-Y-coordinates with the relations

$$x(k,l) = k\Delta R_0 \sin(l\Delta\alpha), \qquad (2.19)$$

$$y(k,l) = k\Delta R_0 \cos(l\Delta\alpha). \tag{2.20}$$

2.6.1 Grid Limits The maximum and minimum grid values in the X-dimension for a correct representation of the data can be calculated as

$$x_{min} = R_{0,max} sin(-\alpha_{max})$$

$$x_{max} = R_{0,max} sin(\alpha_{max}).$$
(2.21)

For instance, a maximum angle $\alpha_{max} = 90^{\circ}$ would lead to a grid width of $2 \cdot R_{0,max}$. The maximum and minimum grid values in the Y-dimension are:

$$y_{min} = -R_{0,max}cos(\alpha = 0) = -R_{0,max}$$

 $y_{max} = R_{0,max}cos(\alpha = 0) = R_{0,max}$. (2.22)

This can also be observed in Figure 2.19. It is proposed that the minimum value for the Y-axis be set to $y_{min} = 0m$ in order to exclude values that are behind the sensor and therefore not relevant.

The locations (x(k,l), y(k,l)) are somewhere in the limits of x_{min} , x_{max} , y_{min} and y_{max} . The definition of the bin size of the grid will allow the formulation of an algorithm for mapping the locations.

2.6.2 Grid Bin Size The dimensions of the bins in the X-dimension Δx and the Y-dimension Δy can be calculated by identifying the smallest distance between the data points. Due to the arc-like arrangement of the data points, these distances are often small, leading to image resolutions that are impractically high.

Therefore the image resolution $N_x \times N_y$ should be static so that its grid spans from x_{min} and y_{min} to x_{max} and y_{max} with the bin sizes

$$\Delta x = \frac{x_{max} - x_{min}}{N_x} \,, \tag{2.23}$$

$$\Delta y = \frac{y_{max} - y_{min}}{N_y} \,. \tag{2.24}$$

2.6.3 Transformation A point in the grid will be referred to with the discrete indexes (n_x, n_y) . Now every point (k, l) corresponds to a point (n_x, n_y) following the condition (see figure 2.18)

$$[n_x \Delta x \le x(k, l) < (n_x + 1)\Delta x] \land [n_y \Delta y \le y(k, l) < (n_y + 1)\Delta y]$$

$$= [X \text{ condition}] \land [Y \text{ condition}].$$
(2.25)

This can be realized using logical masks. When the radar parameters are not changed, the transformation instructions can be reused, because the grids do not change.

For each point (k, l) a corresponding logical mask needs to be applied and the point value $S_B(k, l)$ will be added to the corresponding point in the X-Y-image.

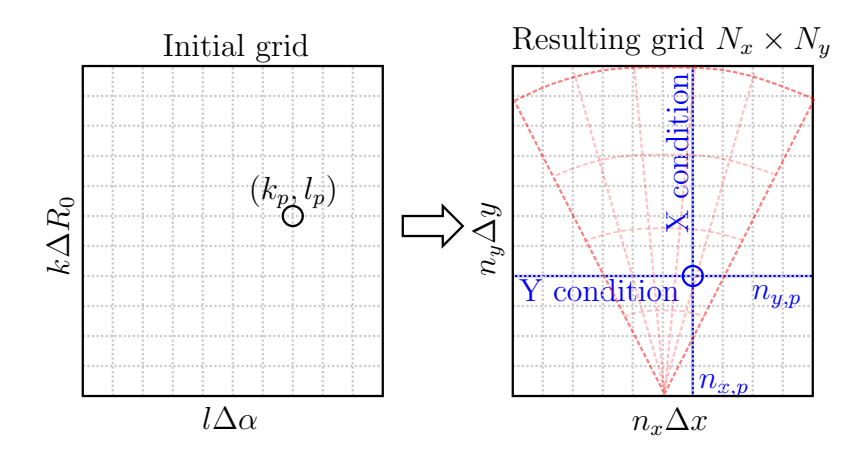


Figure 2.18: Mapping of grid points to the X-Y domain.

2.6.4 Transformation Characteristics Figure 2.19 shows effects that need to be considered when analyzing the transformed image:

- 1. For short distances multiple grid values from $S_B(k,l)$ will be compressed into one grid point in $S_B(x,y)$. If that is the case, the values will be added up.
- 2. For higher distances, the opposite is the case. So some grid points in $S_B(x,y)$ will not be assigned a value. A smoothing filter can be employed for better visibility in the image.
- 3. and 4. There are also blind spots in the corners due to the fact that the radar cone cannot exactly fit inside the square X-Y image.

2.7. FOCUSING 21

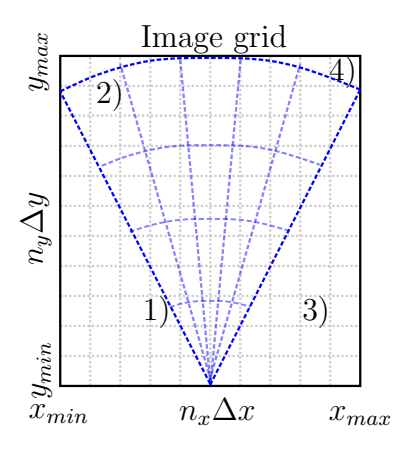


Figure 2.19: The resulting XY-Grid (black) from the range-angle image (blue).

2.7 Focusing

SAR Radars illuminate a set of targets for a period of time while moving. So depending on the chirp duration and chirp sequence duration the relative angle α and the relative distance R_0 become time-dependent. According to equations 2.11 and 2.12 a change in range and angle leads to a range of observed frequencies. This phenomenon is analogous to the smearing observed in long exposure shots captured by a moving camera. The migration of the target into other grid points results in the smearing being referred to as range migration and angle migration. The migration effect is illustrated in figure 2.20. The application of focusing can mitigate this effect in specific areas of the image. [3][11]

2.7.1 Migration prediction Knowing the platform movement allows for the prediction of changes in distance and angle to a point in the image at each time stamp. This point is the focus point with coordinates x_F, y_F . The distance and angle to the focus point are (see figure 2.21)

$$R_F(m,n) = \sqrt{(x_P(m,n) - x_F)^2 + (y_P(m,n) - y_F)^2}$$

$$\alpha_F(m,n) = \arcsin\left(\frac{x_F - x_P(m,n)}{R_F(m,n)}\right).$$
(2.26)

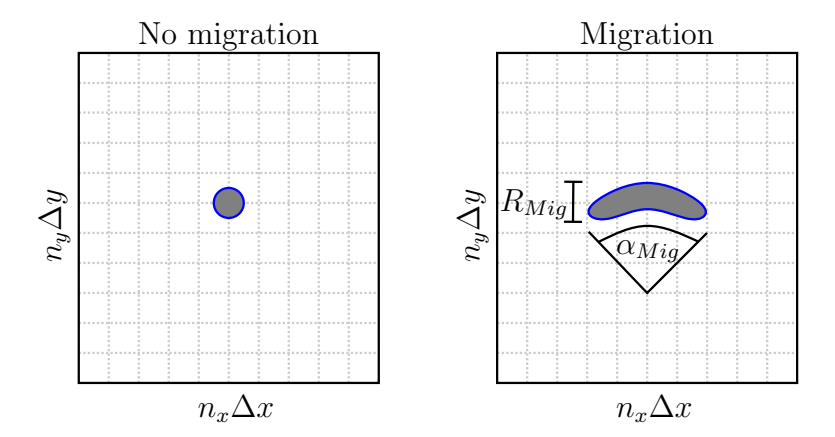


Figure 2.20: A possible result of range and angle migration caused by platform movement.

where x_P and y_P denote the sensor platform coordinates. The change in distance and range from the start of the measurement to the focus point can then be described as the difference between initial and actual values

$$R_{Mig}(m,n) = R_F(m=0, n=0) - R_F(m,n)$$

$$\alpha_{Mig}(m,n) = \alpha_F(m=0, n=0) - \alpha_F(m,n).$$
(2.27)

This change in range and angle is the migration effect. The range migration

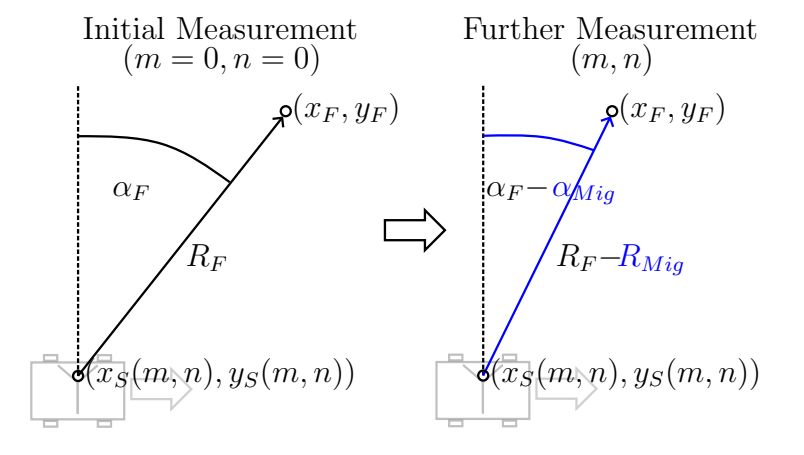


Figure 2.21: A change of the platform position leads to a change in angle and distance to the focus point.

2.7. FOCUSING 23

 $R_{Mig}(m, n)$ and angle migration $\alpha_{Mig}(m, n)$ lead to a set of frequencies that cause smearing in the spectrum and therefore in the image (see equations 2.5 and 2.6).

$$f_{\tau,Mig}(m,n) = -\frac{B_{sw}}{T_{chirp}} \frac{2R_{Mig}(m,n)}{c}$$

$$f_{D,Mig}(m,n) = -f_0 \frac{2v_P sin(\alpha_{Mig}(m,n))}{c}$$
(2.28)

So the baseband signal with migration effects and only one target at the focus point is (see equation 2.4)

$$s_{B,Mig}(m,n) \approx e^{j2\pi([f_{\tau} + f_{\tau,Mig}(m,n)]mT_r + [f_D + f_{D,Mig}(m,n)]nT_{chirp} + \Phi_0)}$$
. (2.29)

It should be noted that multiple targets lead to a sum of baseband signals with migration effects deviating from the focus point.

2.7.2 Migration Correction Again, $f_{\tau,Mig}(m,n)$ and $f_{D,Mig}(m,n)$ can be predicted for every time stamp. So by multiplying the baseband signal with a correction factor that negates the migration effects, the image will be focused.

$$s_{corr}(m,n) = e^{-j2\pi(f_{\tau,M}(m,n)mT_r + f_{D,M}(m,n)nT_{chirp})}$$
 (2.30)

Multiplying the correction factor with the baseband signal will cancel the migration effects at the focus point.

$$s_{B,corr}(m,n) = s_{B,M}(m,n) \cdot s_{corr}(m,n)$$

$$= e^{j2\pi([f_{\tau} + f_{\tau,M}(m,n) - f_{\tau,M}(m,n)]mT_r + [f_D + f_{D,M}(m,n) - f_{D,M}(m,n)]nT_{chirp} + \Phi_0)}$$

$$= e^{j2\pi(f_{\tau}mT_r + f_DnT_{chirp} + \Phi_0)}$$

$$= s_B(m,n)$$
(2.31)

It should be noted that this procedure will only result in a point in the image with no migration effects. Other areas in the image may also be negatively impacted because the correction factor can contribute to the migration effect there. A deviation from the predicted platform movement causes a less focused image due to the fact that the migration frequencies are not perfectly matched. A concept of the focusing algorithm is illustrated in figure 2.22.

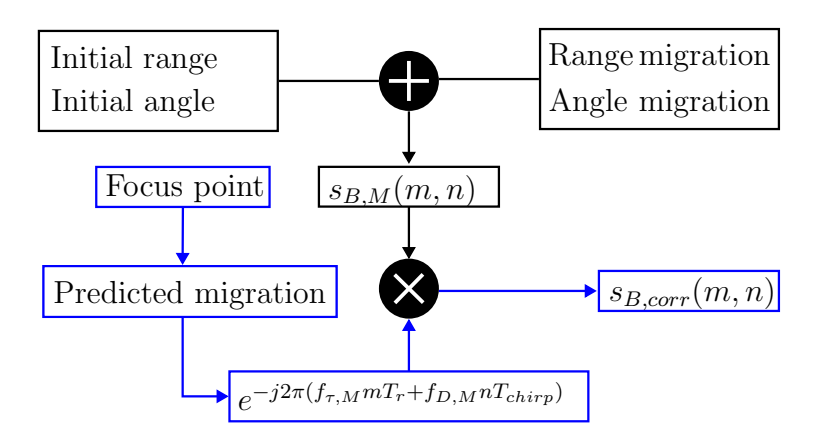


Figure 2.22: Concept of the focusing algorithm.

2.8 Resulting Signal Processing Algorithm

The previously described methods result in a processing algorithm visualized in figure 2.23. The corresponding sections are noted below the icons.

In order to gather the raw data, the radar sensor must emit a suitable chirp sequence waveform. The resulting baseband signal $s_B(t)$ is sampled with a defined rate in both the intra-chirp and inter-chirp dimensions. The data sequence is subsequently arranged as the previously discussed matrix. This results in the baseband signal

$$s_B(m,n) = exp(j2\pi(f_BmT_r + f_DnT_{chirp} + \Phi_0)).$$

Prior to the formation of the image, the raw data must undergo preprocessing. This entails the application of a Dolph-Chebyshev window in both the intrachirp and inter-chirp dimensions, as well as optional focusing to cancel range and angle migration for a specific point in the image.

$$s_{B,preprocessed}(m,n) = s_{B,corr}(m,n) \cdot cheb(m,n)$$

The image formation process involves performing a two-dimensional discrete Fourier transform (DFT). The resulting image grid can be translated into an angle and distance axis.

$$S_B(k,l) = DFT_{m,n}\{s_{B,preprocessed}(m,n)\}$$

To obtain an image in Cartesian coordinates, it is necessary to remap each grid point onto an X-Y grid with a suitable resolution. This conversion can be performed using logical masks.

$$S_B(x,y) \xleftarrow{mapping} S_B(k,l)$$

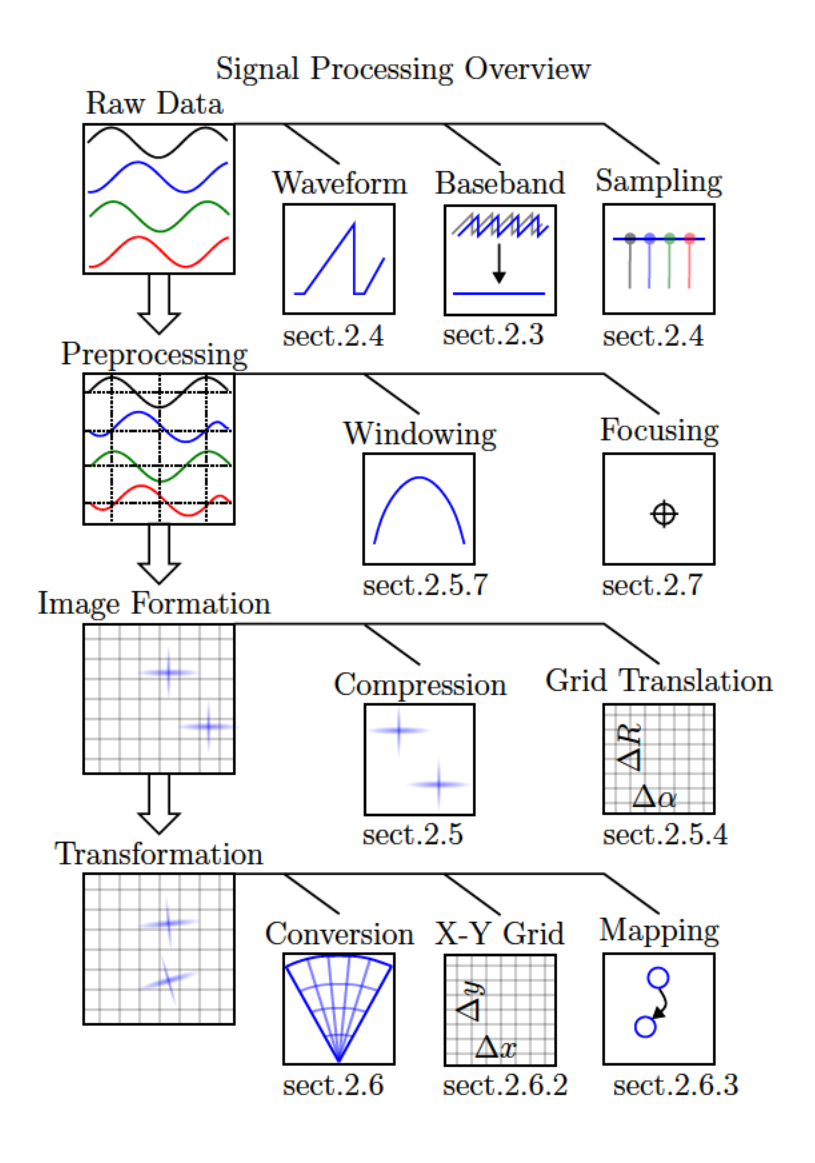


Figure 2.23: Signal processing overview of the proposed SAR algorithm.

Chapter 3

Analysis

After assessment of the employed hardware, the system settings are proposed in section 3.1. These settings are simulated in section 3.2 and tested in section 3.3.

3.1 Hardware and proposed system settings

3.1.1 Radar sensor In this thesis, the radar sensor *IWR6843 ISK* from *Texas Instruments* is used. In combination with the *DCA1000* board from *Texas Instruments*, it is possible to access the raw, unprocessed data from the Radars ADC converters. A detailed description can be found in the cited documentation [12]. This type of data is also simulated and serves as the starting point for signal processing.

For enhanced readability, the simulation and sensor parameters were translated into the aforementioned parameters from the preceding chapter. The proposed configurations are presented in Table 3.1. The interrelationships between these parameters and the sensor and simulation parameters can be found in the appendix (Tables A.1 and A.2). It should be noted that due to the technical limitations of the sensor settings, subsampling is employed in signal processing.

3.1.2 Platform The *Irobot Create 3* automated guided cart (AGC) serves as the sensor platform. In terms of vibration and precision in movement, the platform offers a realistic testing environment, as it is similar to a vacuum cleaning robot in terms of chassis, motorization and wheeling.

Parameter	Description	Value
f_0	Frequency on chirp start	= 60.07GHz
T_r	Sampling time (short)	$=2\mu s$
T_{chirp}	Effective chirp duration	$=256\mu s$
B_{SW}	Effective bandwidth	=1.92GHz
T_{delay}	Time between Chirps	$=5884\mu s$
M	Samples per chirp	= 512
N	Sampled Chirps	=512

Table 3.1: Theory parameters representing the simulation and sensor settings



Figure 3.1: The sensor and platform setup in use.

It is set to a velocity of $v_p = 21 \frac{cm}{s}$ and moves in a straight line. So for one measurement the platform moves for 3.14s and covers a distance of 65.94cm. The sensor is mounted on the top of the platform at a height of 15cm from the ground and facing left in the direction of movement. (see picture 3.1)

3.1.3 Resulting SAR Capabilities With the proposed sensor settings (table A.1 and A.2) and platform speed the maximum unambiguous range is (see equation 2.14)

$$R_{0,max} = \pm 19.94m \tag{3.1}$$

and the size of the range bins is (equation 2.17)

$$\Delta R_0 = 7.79cm. \tag{3.2}$$

3.2. SIMULATION

29

And using equation 2.15 the maximum unambiguous angle becomes (including subsampling)

$$\alpha_{max} = \pm 75.22^{\circ} \tag{3.3}$$

with an angle bin size of (equation 2.18)

$$\Delta \alpha = 0.29^{\circ} \,. \tag{3.4}$$

So regarding only locations in front of the sensor, the boundaries of the XY-image will be (see equation 2.21 and 2.22)

$$x_{min} = -19.28m$$

$$x_{max} = 19.28m$$

$$y_{min} = 0m$$

$$y_{max} = 19.94m$$

$$(3.5)$$

As explained in section 2.6.2 the image resolution will be set independently from the range and angle bin size to $N_x \times N_y = 512 \times 512$. So using equation 2.23 and 2.24 the bin sizes for the X and Y dimensions are:

$$\Delta x = 7.5cm$$

$$\Delta y = 3.9cm$$
(3.6)

Note that the X-Y grid does not actually indicate the image resolution; rather, it constrains the resolution. The relevant indicator for resolution is the range-angle grid.

3.2 Simulation

The simulation creates an environment with the moving sensor and targets. For every time stamp in the simulation, the distance and angle to the target, as well as the sensor's direction of movement and speed, are known. Using equation 2.4 allows simulating and sampling the baseband signal with the simulation parameters described in table 3.1. The sampled data can then be processed as described in the previous chapter.

3.2.1 Targets Point targets are used to assess the quality of the simulation. A point target is defined as a point in the simulation with no spatial

extension. This results in a single baseband frequency per time stamp, which in turn produces a narrow peak in the spectrum and therefore in the image. Therefore, the presence of wider peaks indicates the presence of negative effects on imaging.

3.2.2 Results A simulation of a single point target is shown in figure 3.3. The point target is located at $x_T = 0m$, $y_T = 5m$. The platform starts at $x_P(t = 0) = 0m$, $y_P(t = 0) = 0m$. (compare with figure 3.2) While the Range compression appears to be sharp the azimuth compression is smeared. This indicates that the angular change over the measurement interval is significant. The target position is correctly retrieved from the simulated signal.

A simulation setup for multiple targets is illustrated in figure 3.2. The results are shown in figure 3.4. Again, the target positions are retrieved correctly. The side lobes of the point targets overlap, as can be seen in the logarithmic plots. When linear scal-

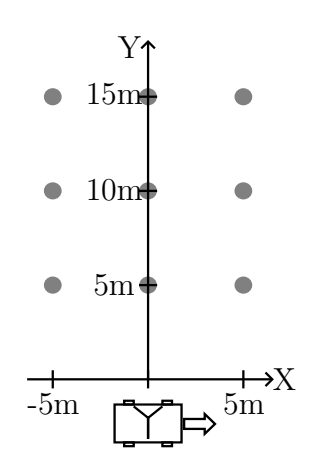


Figure 3.2: Simulation setup for multiple targets.

ing is used, the point targets are sharp and separable. At short distances, the targets appear smeared due to range and angle migration. At longer distances, the targets appear less smeared because the angular change over the measurement interval is less significant.

The focusing procedure is presented in figure 3.5 with the same setup as described in figure 3.2. If the focused point aligns with a target location, the target appears sharp. Targets that are proximal to the focus point also appear sharper than targets that are more distal. As evidenced in image b), the closer the focus point is to the sensor, the more pronounced the smearing for more distant targets becomes. Another consequence of focusing is that the smearing shapes appear to rotate.

3.2. SIMULATION 31

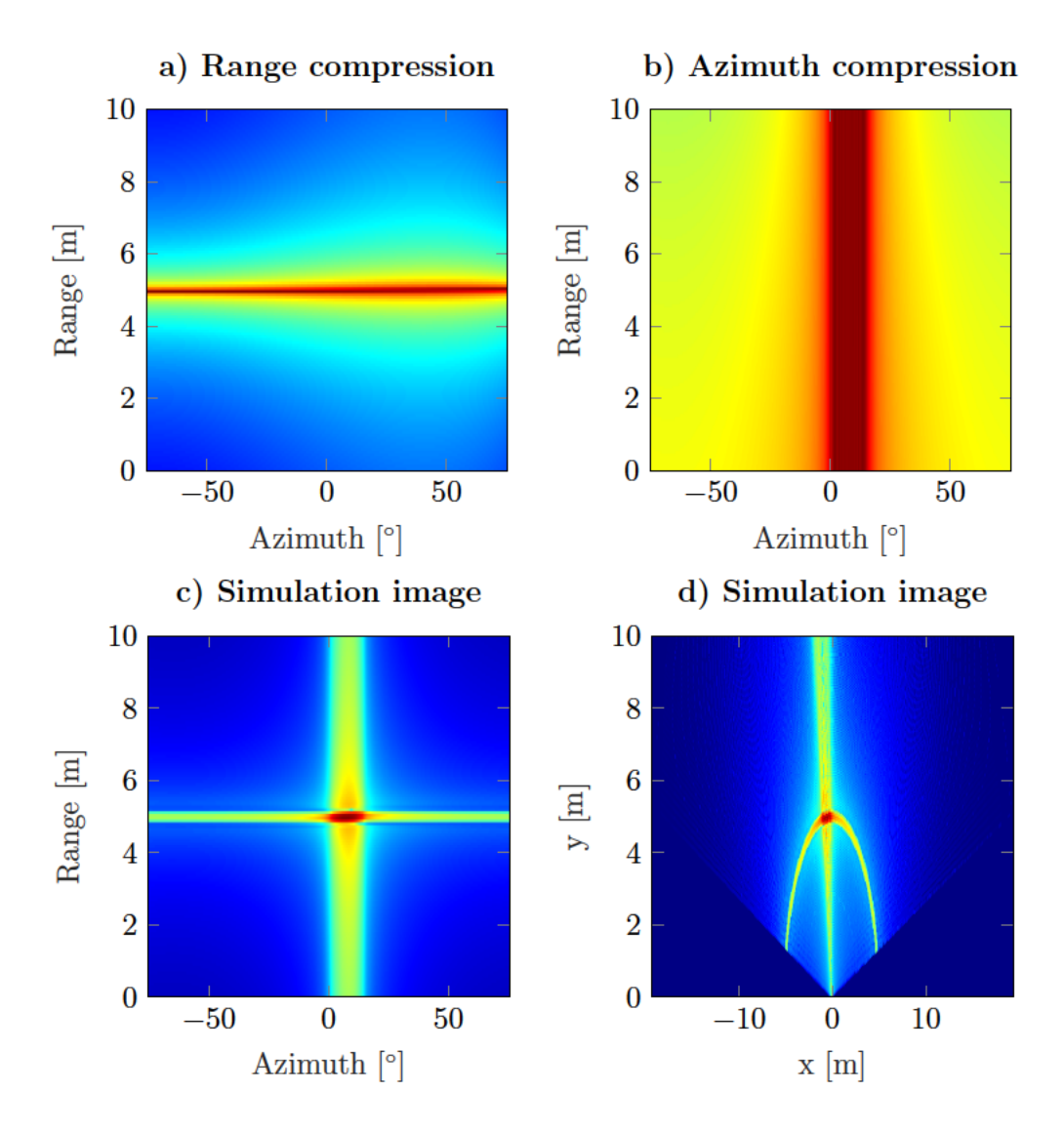


Figure 3.3: Simulation of a single target (logarithmic): a)Range compressed data, b)Azimuth compressed data, c) Range and azimuth compressed data (range-angle image), d) X-Y image.

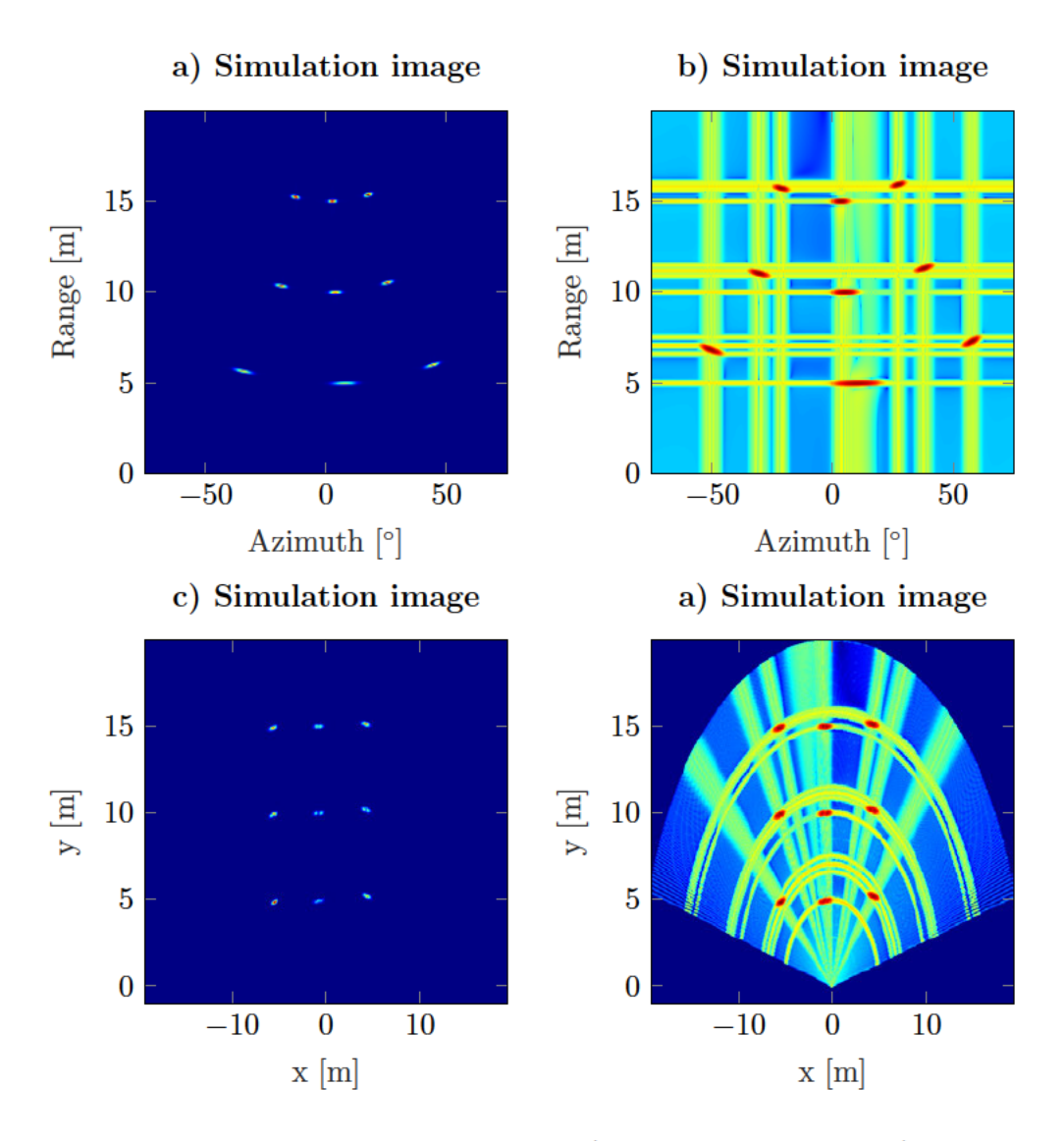


Figure 3.4: Simulation of multiple targets: a) Range-angle image, b) Range-angle image (logarithmic), c) X-Y image, d) X-Y image (logarithmic).

3.2. SIMULATION 33

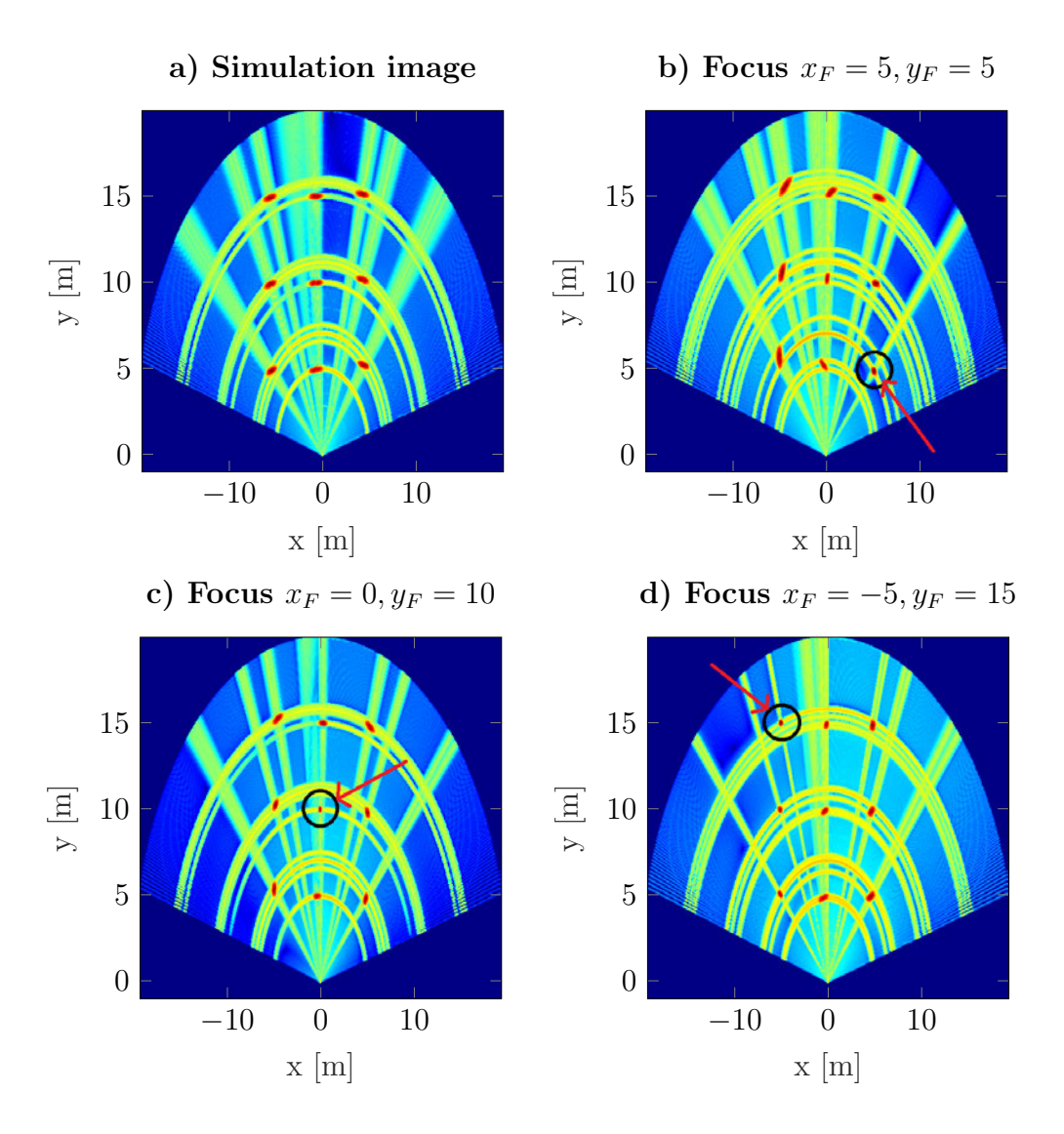


Figure 3.5: Simulation of multiple targets with an a) unfocused image and different focusing points.

3.3 Experimental Results

This section presents the results of experiments designed to test the performance of the imaging algorithm. The first experiment is an entrance hall scenario with minimal clutter. This image is used to assess the algorithm's ability to identify targets. (section 3.3.1)

The second experiment is the imaging of a hallway, which is expected to contain a greater degree of clutter. This image is used to evaluate the algorithm's ability to identify targets in a more challenging environment. (section 3.3.2)

3.3.1 Entrance Hall Measurement In order to test the system with low clutter intensities, an entrance hall with three corner reflectors $(1m^2 \text{ radar cross-section})$ at the y=8.4m line with 3.6m spacing in the x direction is utilized. The image is focused at the coordinates (x=0.8 m, y=8.4 m) to sharpen the central corner reflector. The resulting data can be found in Figure 3.6. A photograph of the entrance hall is provided in Figure 3.6. The result accurately represents the entrance hall from the perspective of the platform's starting position. The corner reflectors do not appear smeared. As a consequence of the low radar cross-section, the columns in the room appear to be of a smaller dimension.

3.3.2 Hallway Measurement A Hallway was selected as a testing environment with high clutter intensity. The result and an illustration of the hallway with the same scale can be found in figure 3.7. Corner reflectors with a radar cross-section of $1m^2$ are used as targets. As illustrated, they were placed 5m, 10m, and 15m away from the sensor (grey circles). There are several metallic door frames and lamp covers that potentially produce clutter.

The shape of the hallway is correctly imaged. All three targets appear as dots at the appropriate locations. No focus was used. There is a considerable amount of clutter at the door frames. Along the left side of the hallway, there is less intense clutter induced by the lamp covers. There are signals from outside the hallway that are indicative of multipath propagation.

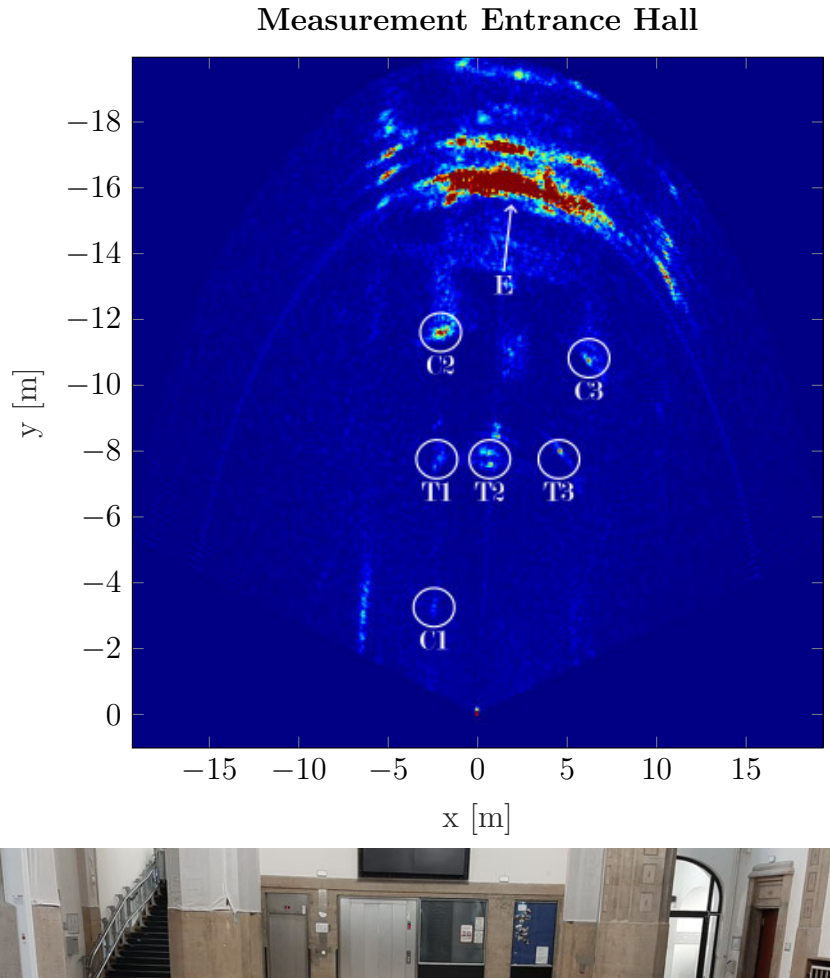




Figure 3.6: Picture and measurement of an entrance hall with landmarks.

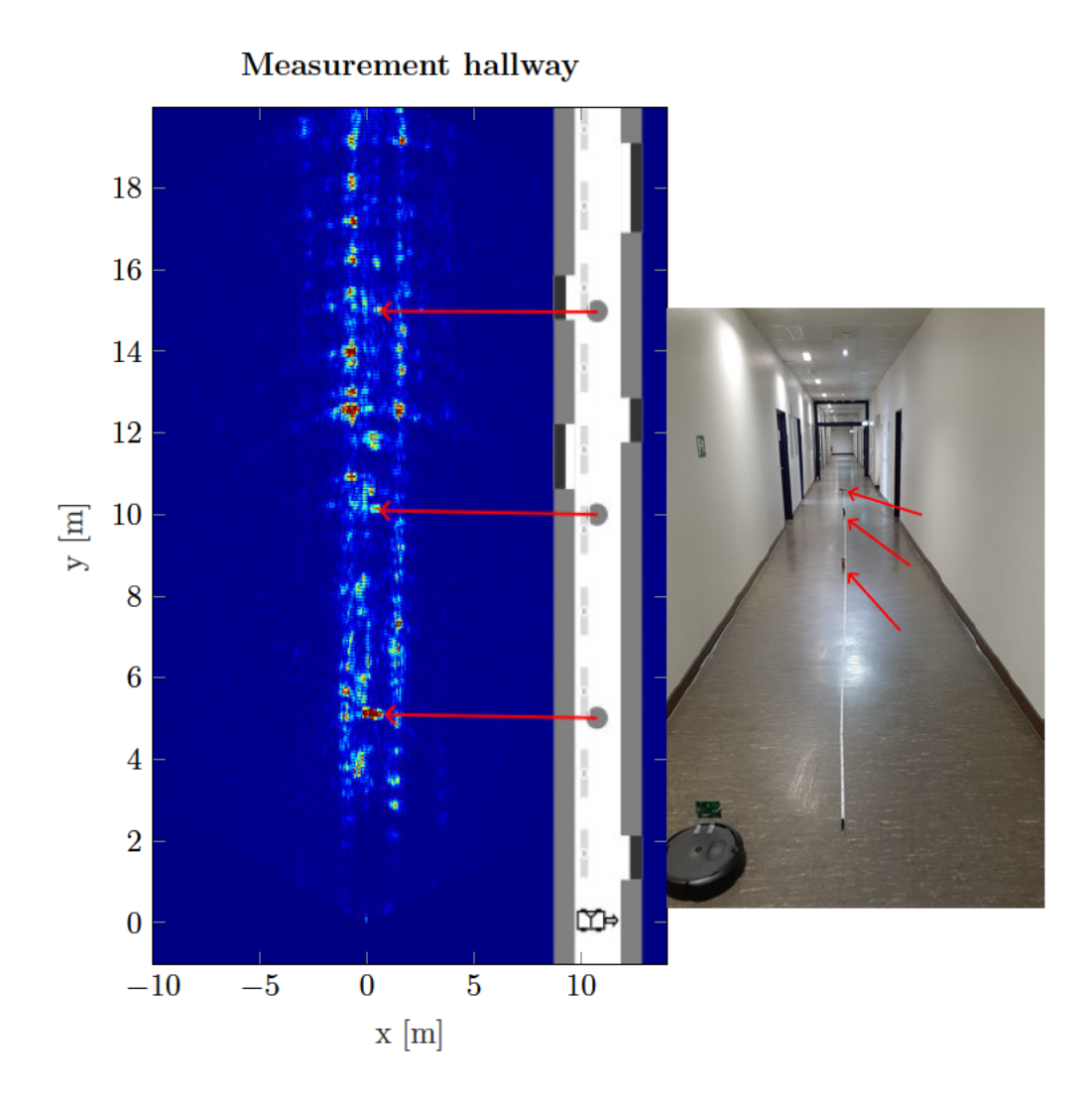


Figure 3.7: Picture, illustration, and measurement result of the Hallway. The corner reflectors are marked with grey dots and highlighted by red arrows.

Chapter 4

Conclusion

This thesis presents a single-input single-output (SISO) synthetic aperture radar (SAR) imaging algorithm and provides a simulation and practical demonstration of its use in an automated guided cart (AGC). The algorithm is capable of achieving sufficient angular and range resolution to create images that resemble the AGC's surroundings even in high-clutter conditions.

All targets appeared at the correct locations on the image. An image range of 19.28m and image angle $\pm 75.22^{\circ}$ is achieved. To generate this, the platform traverses a distance of 66cm in a period of 3.1 seconds, a feat that falls well within the scope of the practical implementation for AGCs. The requisite space for the sensor aperture is minimal, as only one transmitter and one receiver are necessary.

Moreover, the implemented focusing algorithm permits the sharpening of specific image areas, thereby enabling the prioritization of these regions.

The results demonstrate that the SAR method, which has traditionally been employed in the aerospace sector, can be effectively applied to AGCs through the use of SL SISO SAR technology. The objective of this thesis has been successfully achieved.

The presented SAR imaging method is constrained to platform movement in a straight line. To enhance its applicability, it would be beneficial to introduce curved trajectories to the algorithm.

The focusing method presented in this thesis results in a sharpened area of the image but at the cost of worsened smearing in other parts. It would be beneficial to examine the possibility of implementing a multiple-point focusing procedure in order to improve the general image quality, as discussed in reference [11].

Furthermore, the potential for creating multiple differently focused images and subsequent assembly into a single sharpened image should be investigated.

Bibliography

- [1] Fabrizio Torchio. "Survey on automated systems for smart warehouses". PhD thesis. Politecnico di Torino, 2023.
- [2] Adnan Albaba et al. "Forward-Looking MIMO-SAR for Enhanced Radar Imaging in Autonomous Mobile Robots". In: *IEEE Access* 11 (2023), pp. 66934–66948. DOI: 10.1109/ACCESS.2023.3291611.
- [3] Helmut Klausing and Wolfgang Holpp, eds. Radar mit realer und synthetischer Apertur Konzeption und Realisierung. Berlin, Boston: Oldenbourg Wissenschaftsverlag, 1999. ISBN: 9783486598971. DOI: doi: 10.1515/9783486598971. URL: https://doi.org/10.1515/9783486598971.
- [4] Stefano Tebaldini et al. "SAR imaging in automotive scenarios". In: 2022 Microwave Mediterranean Symposium (MMS). 2022. DOI: 10. 1109/MMS55062.2022.9825599.
- [5] Amir Laribi et al. "Performance Investigation of Automotive SAR Imaging". In: 2018 IEEE MTT-S International Conference on Microwaves for Intelligent Mobility (ICMIM). 2018. DOI: 10.1109/ICMIM. 2018.8443554.
- [6] Tang Kan et al. "Implementation of Real-time Automotive SAR Imaging". In: 2020 IEEE 11th Sensor Array and Multichannel Signal Processing Workshop (SAM). 2020. DOI: 10.1109/SAM48682.2020.9104293.
- [7] Sriharsha Nag T S et al. "SAR Imaging with Automotive Radar: Range Migration Algorithm, Experiment, and Future Directions in Automotive Vehicle". In: 2022 IEEE 7th International Conference on Recent Advances and Innovations in Engineering (ICRAIE). Vol. 7. 2022, pp. 382–387. DOI: 10.1109/ICRAIE56454.2022.10054316.

40 BIBLIOGRAPHY

[8] Unal A. Yigit E. Demirci S. "Millimeter-wave Ground-based Synthetic Aperture Radar Imaging for Foreign Object Debris Detection: Experimental Studies at Short Ranges." In: (2012). DOI: 10.1007/s10762-012-9938-2.

- [9] Matthias Kronauge. "Waveform Design for Continuous Wave Radars". PhD thesis. Technische Universität Hamburg-Harburg, 2014. ISBN: 978-3-95404-775-8.
- [10] R. Schilling G. Heinzel A. Rüdiger. Spectrum and spectral density estimation by the Discrete Fourier transform (DFT), including a comprehensive list of window functions and some new at-top windows. 2002. URL: https://hdl.handle.net/11858/00-001M-0000-0013-557A-5.
- [11] Richards M. A. The Keystone Transformation for Correcting Range Migration in Range-Doppler Processing. 2014. URL: https://bpb-us-w2.wpmucdn.com/sites.gatech.edu/dist/5/462/files/2016/12/Keystone.pdf.
- [12] Texas Instruments. Mmwave Radar Device ADC Raw Data Capture. URL: https://www.ti.com/lit/an/swra581b/swra581b.pdf.

Statement of Independence

I hereby declare, that I am the sole author and composer of my thesis and that no other sources or learning aids have been used. However, the *DeepL Write*, *DeepL Translator*, and *Google Grammarly* tools were employed solely for the purposes of language correction and embellishment.

Furthermore, I declare that I have acknowledged the work of others by providing detailed references of said work.

I also hereby declare that my thesis has not been prepared for another examination or assignment, either in its entirety or excerpts thereof.

Hiermit versichere ich, dass ich die vorliegende Arbeit ohne fremde Hilfe selbständig verfasst habe. Zur Sprachkorrektur und -verschönerung der Arbeit wurden jedoch *DeepL Write*, *DeepL Translator*, und *Google Grammarly* genutzt.

Wörtlich oder dem Sinn nach aus anderen Werken entnommene Stellen sind unter Angabe der Quellen kenntlich gemacht.

Desweiteren versichere ich, dass meine Thesis nicht für andere Zwecke verwendet wurde.

Place, date		
Signature		

Appendix A
Sensor settings

Parameter	Name	Description	Setting	Unit
F_0	Start frequency	Frequency on chirp start	60	GHz
T_{RE}	Ramp end time	Chirp duration	390	μs
FS	Frequency slope	Rate of change in frequency over time while chirping	7.5	$MHz/\mu s$
T_{I}	Idle time	Time in between chirps	2670	μs
T_S	Start time	Time before sampling while chirping	10	μs
SR	Sample rate	Samples over time while chirping	2000	$10^3/s$
M	ADC samples	Samples per chirp	512	
NF	No. chirp loops	Chirps per frame	128	
O	No. frames	Count of frames	8	
n_s	Subsampling	Chirps per Sample	2	
T_O	Periodicity	Frame duration	100%	Duty

Table A.1: Proposed sensor parameters

Parameter	Description	Relation
$\overline{n_s}$	Subsampling factor	
f_0	Frequency on chirp start	$= F_0 + FS \cdot T_S$
T_{chirp}	Effective chirp duration	=N/SR
B_{SW}	Effective bandwidth	$=FS\cdot T_{chirp}$
T_{delay}	Time in between	$= (T_{RE} - T_{chirp} + T_I + T_S) \cdot n_s$
	effective chirps	$+(n_s-1)T_{chirp}$
M	Samples per chirp	
N	no. of Chirps	$= NF \cdot O$

Table A.2: Theory parameters and relations to sensor parameters